Eur. Phys. J. E (2012) **35**: 3
DOI 10.1140/epje/i2012-12003-4

THE EUROPEAN PHYSICAL JOURNAL E

Regular Article

Anisotropic Brownian motion in ordered phases of DNA fragments

J. Dobrindt[1,a], E. Rodrigo Teixeira da Silva[2], C. Alves[2], C.L.P. Oliveira[2], F. Nallet[1,b], E. Andreoli de Oliveira[2], and L. Navailles[1]

[1] Université de Bordeaux, Centre de recherche Paul-Pascal – CNRS, 115 avenue du Docteur-Schweitzer, F-33600 Pessac, France
[2] Instituto de Física - Universidade de São Paulo, Rua do Matão, Travessa R Nr. 187, São Paulo, Brasil

Received 17 October 2011
Published online: 24 January 2012 –

Abstract. Using Fluorescence Recovery After Photobleaching, we investigate the Brownian motion of DNA rod-like fragments in two distinct anisotropic phases with a local nematic symmetry. The height of the measurement volume ensures the averaging of the anisotropy of the in-plane diffusive motion parallel or perpendicular to the local nematic director in aligned domains. Still, as shown in using a model specifically designed to handle such a situation and predicting a non-Gaussian shape for the bleached spot as fluorescence recovery proceeds, the two distinct diffusion coefficients of the DNA particles can be retrieved from data analysis. In the first system investigated (a ternary DNA-lipid lamellar complex), the magnitude and anisotropy of the diffusion coefficient of the DNA fragments confined by the lipid bilayers are obtained for the first time. In the second, binary DNA-solvent system, the magnitude of the diffusion coefficient is found to decrease markedly as DNA concentration is increased from isotropic to cholesteric phase. In addition, the diffusion coefficient anisotropy measured within cholesteric domains in the phase coexistence region increases with concentration, and eventually reaches a high value in the cholesteric phase.

1 Introduction

The Brownian motion of colloidal particles consists of continuous random displacements while the particle experiences a friction force with the surrounding solvent. Even though it has been observed in simple systems about two centuries ago, the development in recent decades of new experimental tools and computer simulations have renewed the interest for Brownian motion, with investigations devoted to more complex situations involving concentrated solutions, confined systems or anisotropic colloids. In particular, solutions of rigid rods have been used as model systems to investigate diffusion of polymers, viruses, and anisotropic molecules, leading to applications in biology, chemistry and industry.

From a theoretical point of view, the centre-of-mass displacement of a cylindrical particle in solution is simply characterised in terms of two independent translational friction coefficients, for motions parallel and perpendicular to the cylinder long axis, respectively [1–3]. Experimentally, two regimes of Brownian motion have been observed in isotropic suspensions of rod-like particles. The first regime, corresponding to low volume fractions, is characterised by a diffusion coefficient independent of concentration that is also well described by properly averaging the two basic friction coefficients [4,5]. In the second, more concentrated regime when the particles start to interact, the diffusion coefficient D becomes dependent on the particle volume fraction [4–9], and various theoretical models or numerical simulations [10–15] relevant in this regime have been proposed. At still higher concentrations, the cylinders become orientationally correlated as the nematic phase is reached. The long-time mean square displacement of a single particle is anisotropic [16–21] which explicitly reflects the broken symmetry of the nematic phase, (also observed in the transport properties of thermotropic liquid crystal systems [22, 23]) as well as the difference between the lengthwise and side-ways friction coefficients at the single-particle level. In this case also, numerical approaches and theoretical studies are available [24–26].

Experimentally, real-time optical microscopy has been applied to visualise the displacement of individual long particles [19–21, 27–30] however, for much smaller particles in concentrated solutions, FRAP (Fluorescence Recovery After Photobleaching) techniques are more appropriate and quite powerful [4, 7, 9, 16, 31–33]. The diffusion process can be investigated at the micrometre length

[a] *Present address:* Laboratory of Photonics and Quantum Measurements (SB/STI), École polytechnique fédérale de Lausanne, CH-1015 Lausanne, Confédération helvétique.
[b] e-mail: `nallet@crpp-bordeaux.cnrs.fr`

scale with known and well-defined initial boundary conditions, in principle allowing one to solve the diffusion equations [16,32,34].

In this work we investigate the anisotropic Brownian motion of DNA rod-like fragments using FRAP for aligned samples exhibiting different symmetries. The first system is a ternary DNA-lipid complex swollen with solvent, where a local, two-dimensional nematic order is observed for the DNA fragments confined by lipid bilayers stacked in a lamellar phase. The second system is a binary DNA-solvent mixture in isotropic or cholesteric phases, depending on DNA concentration. We propose a method for analysing isotropic images in order to handle with a local anisotropic diffusion. The experiments are performed with a confocal laser scanning microscope (CLSM) in planar domains of the cholesteric phase, where the helical axis is parallel to the direction of the illuminating light, or in homeotropic domains of the lamellar complex. In such geometries the anisotropic in-plane displacement of the DNA molecules is averaged along the height of measurement volume, resulting in a non-Gaussian shape for the bleached spot as fluorescence recovery proceeds. Nevertheless, the fluorescence recovery can be analytically described in simple but representative limiting cases, and the two distinct translational diffusion coefficients can then be determined.

2 Experimental methods

DNA fragments are prepared from calf thymus DNA provided by Sigma-Aldrich. Ionic impurities present in the raw material are removed by precipitating DNA in a buffer solution (sodium acetate 3 M, *p*H adjusted to 5.2, also from Sigma-Aldrich) mixed with pure ethanol. After freezing overnight, the mixture is centrifugated several times and the supernatant removed. The precipitate is then subjected to lyophilization providing salt-free nucleotides to be sonicated. The cleavage of polynucleotides is performed by sonicating at 35 kHz the DNA solutions. The device delivers 35 W of acoustic power and the total sonication time is about 30 hours. The DNA solutions are cooled by immersion in a water bath containing a mixture of liquid water and ice in order to prevent excessive heating during such a lengthy process. At the end of the process, gel electrophoresis reveals DNA pieces of *ca.* 150 base pairs, or a contour length L around 50 nm, *i.e.* the DNA persistence length: the DNA fragments are thus appropriately described as being rod-like, with an actual diameter Φ about 2 nm without taking into account the hydration shell. The fluorescent dye YOYO-1 —product code Y3601 from Invitrogen, Carlsbad, USA— is then intercalated at an overall ratio of 1 dye molecule for every 5000 base pairs.

For preparing the binary system, it is important to precisely control the ionic strength and *p*H of the DNA aqueous dispersion. The de-ionised material is mixed in known amounts with a 0.25 M buffer solution of ammonium acetate at (measured) *p*H = 7.0. The sample concentrations (respectively, volume fractions) are chosen in the range 80–350 mg/mL (respectively, 4.7–17%, taking as nominal value for the DNA fragment density $\rho = 1.7$ g/mL). According to previous observations on a similar system [35,36], this range spans the (concentrated) part of the isotropic domain of the phase diagram, a complex phase coexistence region where cholesteric domains can be found, and the one-phase cholesteric domain. Though already fairly concentrated, our 350 mg/mL sample is thus not expected to lie beyond the cholesteric-to-columnar phase boundary [36], as confirmed by its characteristic cholesteric texture that was observed with polarising microscopy —data not shown. On the other hand, our most dilute sample lies well within the semi-dilute region of the isotropic domain and is correspondingly somehow viscous since its nominal volume fraction is more than an order of magnitude larger than the overlap volume fraction ϕ^*, here estimated from the relation $\phi^* \approx 1.5 \times (\Phi/L)^2$ to be about 0.24%.

The lipid host phase for DNA in the ternary DNA-lipid complex is prepared by adding pure water to a mixture of a zwitterionic lipid (soya lecithin-phosphatidylcholine headgroup or PC, purchased from Sigma) and a cosurfactant (simulsol, a mixture of ethoxylated fatty acids derived from oleic acid (71%) and palmitic acid (11%) as main components, purchased from Seppic), with the PC/simulsol mass ratio kept constant and equal to 7/3. A lamellar structure of periodically stacked fluid bilayers with thickness of *ca.* 3.7 nm is obtained at room temperature over a broad range of water contents [37–39]. The ternary DNA-lipid complex is obtained by thoroughly mixing DNA fragments (prepared as described above), lipids and solvent. With DNA-to-lipid volume ratio equal to 3.1 and solvent volume fraction in the range $0.3 \leq \phi_w \leq 0.4$, the DNA fragments are orientationally ordered in a nematic fashion within each solvent layer, but without correlations between nematic directors across the one-dimensionally stacked bilayers [37–39]. The period d of the lamellar stack always remains close to 7 nm.

The fluorescence recovery after photo-bleaching (FRAP) experiment is performed with a confocal laser scanning microscope (Leica TCS SP2, Germany) allowing surgical bleaching [32]. The general principle of the technique is to (nearly) instantaneously and irreversibly bleach a localised region within the fluorescently labelled sample by irradiating it with a short and intense light pulse. In the specific case of surgical bleaching as used here, the bleach is not performed by scanning an *extended* region of interest. Instead, it is carried out within a "point-like" geometry. In the present experiment, we are using the 488 nm line of an argon laser, as this wavelength is very close to the excitation peak of the dye, namely 491 nm. Shortly after irradiation, usually within 300 ms, a highly attenuated light beam, scanned along the lines of a (square) region of interest surrounding the bleached area is used to measure the recovery of fluorescence (detection spectral bandwidth 500–600 nm) as a result of diffusion exchanges between bleached and unbleached fluorophores.

Sample drops are deposited onto glass slides and rapidly covered with glass coverslides. A gentle shearing is manually realised for a few seconds. The cells are then sealed with a UV-curing glue (NOA81 from Epotecny, France) to prevent solvent evaporation. Owing to this procedure, the cell thickness e along the microscope optical axis is not precisely known, but lies in the range $5-15$ μm. Some samples are also occasionally prepared in flat glass capillaries (VitroCom, NJ, USA) with optical path 50 or 100 μm, sealed with glue, in those cases where a too small viscosity would have led to too thin samples if using the first method.

For the cholesteric sample, or samples in the complex phase coexistence region exhibiting cholesteric domains, planar anchoring (with DNA molecules on average parallel to the glass flat sides —(x, y)-plane— or, equivalently, the helical axis being parallel to the set-up optical axis z) is favoured by the shearing motion. Well-oriented domains of a few hundred micrometre sizes are easily obtained, as checked using polarising microscopy. From previous work [40], the helical pitch in the cholesteric phase is expected to be in the order of $p = 2$ μm, as its strong increase with DNA concentration occurs only close to the cholesteric-to-columnar phase boundary. In all our experiments, the number of helical turns from the lower to the upper flat side of the cell, e/p, is thus always significantly larger than 1. With the DNA-lipid system, the favoured anchoring corresponds to bilayers being parallel to the glass flat sides (or "homeotropic" anchoring). In homeotropically oriented domains, the stacking axis is therefore also parallel to the set-up optical z-axis. The number of stacked solvent layers across the height of the cell is typically in the order of 10^3 or more.

The acquisition of a data series involves recording (usually ten) background images prior to bleaching, followed by a localized, "point-like" bleaching for one second. Shortly after the end of the bleaching step, images at times t_n are recorded and the averaged background is subtracted. In order to properly establish the origin of the appropriate polar coordinate system (which would be specially relevant in the case of *anisotropic* in-plane diffusion), the centre of the bleached spot is located by a search algorithm adapted from ref. [32]: each image is scanned in the square window corresponding to the region of interest and the centre of rotational symmetry is determined by minimizing the difference between the image and a transformed one obtained by a 90° rotation around the searched centre. The method does not require any previous knowledge about the orientation of the diffusion principal axes in the image plane, especially when multiple vertically stacked profiles are averaged in one image, but is useful for increasing the signal-to-noise ratio: At each time t_n the image is azimuthally averaged around its symmetry centre. The resulting trace is analysed using a fit model described in sect. 3.1, where it appears that the vertically stacked profiles averaging process is of crucial significance. The vertical averaging process actually results form the fact that the bleaching and imaging are performed on a confocal microscope equipped (in most cases) with a 10× objective, numerical aperture NA 0.3, sometimes with a 40× objective, numerical aperture NA 0.6. The diffraction-limited diameter of the Airy disk at $1/e^2$ intensity is therefore 1.4 and 0.7 μm, respectively, with a corresponding depth of field estimated from paraxial Gaussian optics (see sect. 3 below) to be 6 and 1.6 μm, respectively, comparable to but not always much larger than the sample thickness. In order to ensure a satisfactory azimuthal averaging of the diffusion properties across the height of the observed domains, opening the aperture diaphragm in front of the detection system and, therefore, decreasing the axial resolution is necessary for experiments with the 40× objective. It is also useful for increasing the measured intensities.

3 Diffusion model and data analysis

3.1 Theoretical framework

The depletion in fluorescence intensity at the in-plane distance r and azimuthal coordinate θ relative to the centre of the axially symmetric bleached spot, after a time t has elapsed from the (infinitely short, but spatially extended) bleaching pulse, $F_0(r, \theta, t)$, is related to the concentration of bleached molecules, $c(r, \theta, z, t)$, by the relation

$$F_0(r, \theta, t) = \mathcal{N}_0 \int_{-Z/2}^{+Z/2} \mathrm{d}z \; \mathrm{PSF}(z)\, c(r, \theta, z, t), \qquad (1)$$

where PSF is the optical system point spread function, z a coordinate along the microscope optical axis ($z = 0$ corresponds to the focal plane of the microscope) and Z the height of the observed bleached zone (with a possible cut-off given by the axial resolution of the microscope), $\mathcal{N}_0$ being a scaling/normalisation constant. Note that, in writing eq. (1), we neglect the in-plane effect of the point spread function, as it only induces a small offset in the full width at half maximum (FWHM) of a concentration profile already widened by diffusion.

In the simple case originally considered by Seiffert and Oppermann for spatially resolved FRAP in a CLSM [32], integration along z is irrelevant because both the incident bleaching light intensity and the fluorophore transport properties are translation-invariant along this direction. This is still the case for the more complicated situation, already considered in ref. [33], where the fluorescent molecules are confined in the narrow water layers of a (homeotropically oriented) lyotropic lamellar phase: Even though fluorophores confined within different layers are dynamically decoupled (permeation through lipid bilayers being negligible), the absence of any in-plane symmetry axis allows the recovery of translational invariance along z. The two cases we are interested in here are quite different, however. For a cholesteric phase with its helical axis along z, the (local) nematic director rotates as height changes, which leads to in-plane motions with a z-dependent anisotropy. For a DNA-lipid lamellar complex with a (2d) nematic order for the DNA molecules,

in-plane Brownian motions are, similarly, anisotropic. Significant differences with the above-mentioned cholesteric case, however, are worth mentioning: i) Brownian motion of the fluorophores along z can be neglected, and ii) there are no *a priori* correlations between local nematic axes for layers at distinct heights.

Because the fluorophore transport properties are no longer translation-invariant along z, the integration expressed by the convolution with the point spread function in eq. (1) has to be considered *explicitly*. Still, if the integration range Z is large enough along the helical or stacking axis (cholesteric system or DNA-lipid lamellar complex, respectively) F_0 in eq. (1) should not actually depend on coordinate θ. Considering the present capabilities of confocal laser scanning microscopes, the validity of the assumption is granted for usual lyotropic lamellar phases with a stacking period typically less than 10 nm, but, as already mentioned, may require operating the CLSM *without* ensuring confocality during the readout of the fluorescence in the bleached region for a cholesteric phase with a pitch about 2 μm.

Generally speaking, the spatio-temporal dependence of the concentration field is to be determined from the anisotropic form of Fick's diffusion equation appropriate for the system under consideration, given initial conditions arising from the bleaching pulse. There are no special difficulties expected when considering the DNA-lipid lamellar complex with 2d nematic order, but a cholesteric liquid crystal deserves special care. On symmetry grounds, such a system should behave in the long-wavelength, low-frequency limit as a smectic A liquid crystal, *i.e.* similarly to the case studied in ref. [33] but, as noted long ago in ref. [41], it is far from clear that the hydrodynamic description of diffusion is appropriate for a cholesteric liquid crystal at the wavelengths and frequencies of practical interest here. A somehow similar difficulty was encountered in the work described in ref. [19] where the cholesteric phase of the rod-like *fd* virus was analysed as if it were actually non-chiral, *i.e.* nematic.

In the following, and with the aim of simplifying the analysis, we *assume* the decoupling of axial and in-plane relaxations, therefore describing the diffusion dynamics in independent and stacked "slices", each with a local two-dimensional nematic symmetry. Within a given slice, the diffusion tensor is diagonal, with values $D_\parallel$ and $D_\perp$ along and perpendicular to the local nematic director, respectively. Though innocuous for the DNA-lipid lamellar complex (because of a negligible permeation), such an assumption is in principle questionable for the cholesteric system. It is expected to hold true only if axial concentration gradients remain at all times much smaller than in-plane concentration gradients[1].

In a properly chosen Cartesian coordinate system, and for a given slice at height z, the diffusion equation writes

$$\partial_t c(\mathbf{r},t) = \left[D_\parallel \partial_{x^2} + D_\perp \partial_{y^2}\right] c(\mathbf{r},t). \tag{2}$$

[1] Note that the same restriction applies in principle even to the usual case of an isotropic system.

For a concentration profile initially strongly localised along the symmetry axis, that is to say with a projection onto the (x,y)-plane proportional at time 0 to a δ-function, the standard solution is $c_\delta(\mathbf{r},t)$

$$c_\delta(\mathbf{r},t) = \frac{c_0(z)}{4\pi t\sqrt{D_\parallel D_\perp}} \times \exp\left(-\frac{x^2}{4D_\parallel t}\right)\exp\left(-\frac{y^2}{4D_\perp t}\right), \tag{3}$$

with $c_0(z)$ the concentration of photobleached molecules per unit length, *i.e.* integrated in the (x,y)-plane.

In local polar (cylindrical) coordinates (r,ϕ) with the origin for the azimuthal angle taken along the *local* nematic director, eq. (3) becomes

$$c_\delta(r,\phi,z,t) = \frac{c_0(z)}{4\pi t\sqrt{D_\parallel D_\perp}} \times \exp\left(-\frac{r^2\cos^2\phi}{4D_\parallel t}\right)\exp\left(-\frac{r^2\sin^2\phi}{4D_\perp t}\right). \tag{4}$$

In the laboratory frame, local polar coordinates transforms into (r,θ) with $\theta = \phi + 2\pi z/p$ to account for the helical winding with pitch p of the nematic director along z (cholesteric system), or $\theta = \phi + \alpha(z)$, with $\alpha(z)$ an arbitrary function of z (DNA-lipid lamellar complex). The depletion in fluorescence intensity is thus given by the following integral:

$$F_0(r,t) = \mathcal{N}_0 \int_{-Z/2}^{Z/2} \mathrm{d}z\, \mathrm{PSF}(z)\frac{c_0(z)}{4\pi t\sqrt{D_\parallel D_\perp}} \times e^{-\frac{r^2\cos^2(\theta-2\pi z/p)}{4D_\parallel t}} e^{-\frac{r^2\sin^2(\theta-2\pi z/p)}{4D_\perp t}}, \tag{5}$$

where we have chosen, for illustration purposes, to focus the remaining part of the derivation on the cholesteric system. The other case leads to a wholly similar result if one replaces, when appropriate, $2\pi z/p$ by $\alpha(z)$ and references to "helical pitch" by the length scale —10 to 100 times the stacking period, presumably— along which the function $\alpha(z)$ uniformly samples the interval $[0, 2\pi]$.

In order to proceed further, we make now the specific assumption that the variations along z of the concentration $c_0(z)$, as well as of the point spread function $\mathrm{PSF}(z)$ are slow at the scale given by the helical pitch, which amounts to writing the intensity as

$$F_0(r,t) \approx \mathcal{N}_0 \sum_{n=-N}^{N} \mathrm{PSF}(Z_n)c_0(Z_n)\int_{-p/2}^{p/2}\mathrm{d}z\frac{1}{4\pi t\sqrt{D_\parallel D_\perp}} \times e^{-\frac{r^2\cos^2(\theta-2\pi z/p)}{4D_\parallel t}} e^{-\frac{r^2\sin^2(\theta-2\pi z/p)}{4D_\perp t}}, \tag{6}$$

where Z_n is the average location of the n-th slice of thickness p along the height of the bleached volume, the number of terms in the sum, namely $2N+1$, being given by the ratio Z/p. This expression readily transforms into

$$F_0(r,t) = \mathcal{N}_1 \frac{1}{4\pi t\sqrt{D_\parallel D_\perp}} \times \exp\left[-\frac{r^2}{8t}\left(\frac{1}{D_\parallel}+\frac{1}{D_\perp}\right)\right] \times \mathrm{I}_0\left[\frac{r^2}{8t}\left(\frac{1}{D_\parallel}-\frac{1}{D_\perp}\right)\right], \quad (7)$$

where $\mathcal{N}_1$ is a scaling constant that includes the sum

$$\sum_{n=-N}^{N} c_0(Z_n) \quad (8)$$

and I_0 denotes the modified Bessel function of the first kind and integer order 0.

As expected in view of our starting hypotheses, the obtained expression for the depletion in fluorescence intensity no longer depends on the azimuthal in-plane coordinate θ. Still, its non-Gaussian shape as a function of the radial coordinate r captures the required information relative to the diffusion coefficient *anisotropy*. This is our central result, to be used in analysing the FRAP data in the following section.

3.2 Initial conditions

The initial concentration of bleached molecules is of course not singular at $r = 0$ in actual experiments. The concentration field at $t = 0$ is usually considered to be proportional to the bleaching light intensity [42], which yields a simple profile when using a laser. Indeed, if the objective has a low numerical aperture, as typically used in spatially resolved FRAP experiments [32,43], the paraxial approximation is appropriate to describe the Gaussian light intensity profile —here taken as an idealised model for the actual illuminating profile in the experiment. This leads to

$$w(z) = w_0\sqrt{1+\left(\frac{z}{z_R}\right)^2} \quad (9)$$

for the beam in-plane half-width at e^{-2} intensity and to

$$I(z) = I_0\left[\frac{w_0}{w(z)}\right]^2 \quad (10)$$

for the beam axial intensity profile, with the characteristic length (Rayleigh range) z_R related to the beam waist w_0 and wavelength of the light λ by $z_R = \pi w_0^2/\lambda$.

Such a more realistic description of the initial conditions for the diffusion problem amounts to replacing the concentration field in eq. (4) by the following, very similar form:

$$c(r,\phi,z,t) = \frac{c_0}{2\pi\sqrt{(R^2+2D_\parallel t)(R^2+2D_\perp t)}} \times e^{-\frac{r^2\cos^2\phi}{2R^2+4D_\parallel t}} e^{\frac{r^2\sin^2\phi}{2R^2+4D_\perp t}}, \quad (11)$$

with a (z-dependent) initial standard deviation R equal to $w(z)/2$, and c_0 a constant proportional to I_0.

The integration along the optical axis as in eqs. (5) and (6) remains to be performed. If the integration range Z were small enough in comparison with the Rayleigh range z_R and centred at the beam waist plane, eq. (7) would be simply replaced by

$$F_0(r,t) = \mathcal{N}_2 \frac{1}{\pi\sqrt{(w_0^2+8D_\parallel t)(w_0^2+8D_\perp t)}} \times \exp\left[-r^2\left(\frac{1}{w_0^2+8D_\parallel t}+\frac{1}{w_0^2+8D_\perp t}\right)\right] \times \mathrm{I}_0\left[r^2\left(\frac{1}{w_0^2+8D_\parallel t}-\frac{1}{w_0^2+8D_\perp t}\right)\right], \quad (12)$$

with $\mathcal{N}_2$ a scaling constant including the focal plane value of the point spread function $\mathrm{PSF}(z = 0)$. The non-Gaussian characteristics of the FRAP profile at finite t, already found in eq. (7), would thus be recovered but with a less restrictive initial condition.

For the general case where Z may be comparable to, or larger than z_R, it is unfortunately no longer possible to express in a closed form the depletion in fluorescence intensity at all times, and not even at $t = 0$. In the long-time limit, however, the diffusion length scale, *i.e.* here the smaller of $D_\parallel t$ and $D_\perp t$, is ultimately much larger than the Gaussian beam intrinsic scales (w_0, λ and z_R). The simple form of eq. (7) is therefore *asymptotically* recovered, as argued in sect. 3.3 below. In sect. 4, we will then use for convenience the closed form (possibly non-rigorous at short times) expression given by eq. (12) for extracting anisotropic diffusion coefficients. The observable *non*-Gaussian shape of the concentration profile at (and close to) $t = 0$ is attributed to the above-described imperfections of our model.

3.3 Numerical simulations

To check the integrity of our model, we simulate anisotropic diffusion on a 2d mesh, using a finite element method within the MATLAB Partial Differential Equation Toolbox, and generate data for different initial bleaching conditions that is processed as described in sect. 2 for experimentally recorded images. We use i) a circular Gaussian profile, and ii) (axially symmetric) initial conditions that are given by the difference of two exponential integral functions

$$E_1\left(\frac{r^2}{2R_>^2}\right) - E_1\left(\frac{r^2}{2R_<^2}\right). \quad (13)$$

In eq. (13), the mismatch between the two lengths $R_>$ and $R_<$ (with $R_> > R_<$) controls the flattening of the profile, a practically useful feature as flatter shoulders are sometimes encountered in the experiment.

The simulated traces are analysed using a fit function proportional to

$$\exp\left[-r^2(a^{-1}+b^{-1})\right] \times \mathrm{I}_0\left[r^2(a^{-1}-b^{-1})\right] \quad (14)$$

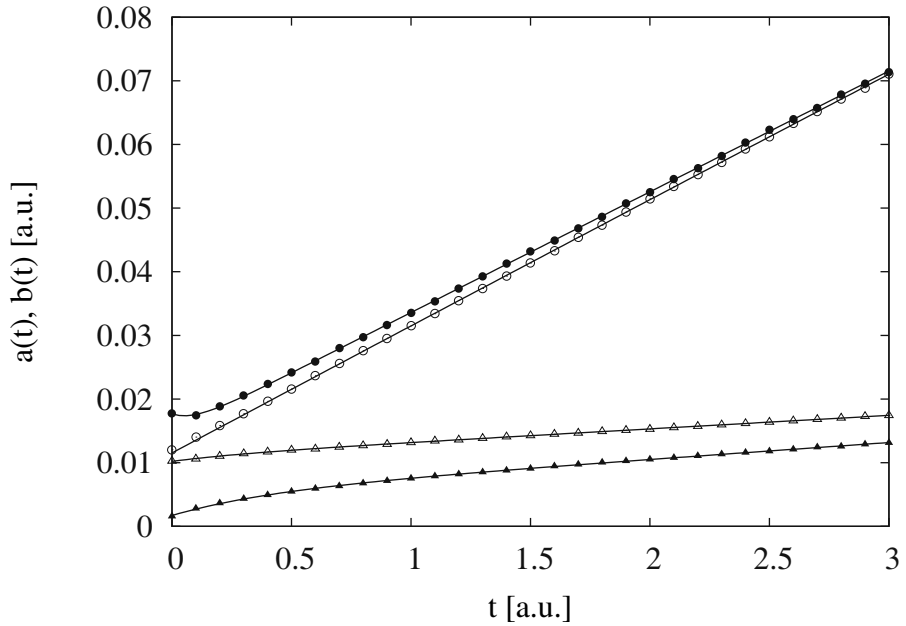

Fig. 1. Increase in time of the fit parameters $a(t_n)$ and $b(t_n)$ in eq. (14) ($\circ$ or $\bullet$: along the quick axis $\|$; $\triangle$ or $\blacktriangle$: along the slow axis $\perp$) derived from anisotropic diffusion simulations for different initial bleaching profiles (Gaussian: open symbols $\circ$ and $\triangle$, and Exponential-Integral: filled symbols $\bullet$ and $\blacktriangle$). The solid lines represent fits using the model $p_0 + p_1 t + p_2 e^{-p_3 t}$. The diffusion coefficients are derived from the linear contribution p_1.

built from eq. (12) of our model. The obtained fitting parameters a and b for an anisotropy ratio $D_\|/D_\perp = 10$ are depicted as a function of time in fig. 1. The linear contribution, and thus the diffusion constants, can be extracted by fitting a and b with an exponential decay function added to a linear background. In arbitrary units, the chosen values $D_\| = 20$ and $D_\perp = 2$ are well reproduced in the case of Gaussian initial conditions ($D_\| = 19.01$ and $D_\perp = 2.12$) and slightly worse for the Exponential-Integral case ($D_\| = 18.97$ and $D_\perp = 2.64$, all values extracted from fits in fig. 1). Similar results are obtained for simulations with different anisotropy ratio, namely $D_\|/D_\perp = 2$, 3 or 4. This indicates that any departure from the Gaussian profile at, or close to $t = 0$ is not critical in determining the diffusion coefficient anisotropy, as long as the asymptotic linear behaviour can be extracted from the data.

Incidentally, we note that the method described in sect. 3 allows a stable analysis of anisotropic diffusion also in the case of translational invariance along the z-axis, where an elliptic (as opposed to circular) profile should be visible. In the method that we propose, the 2d analysis of the data is reduced to a 1d fit by the azimuthal averaging procedure, while at the same time information about the rotation angle between laboratory and local polar (cylindrical) coordinates is lost. This simplification comes at the cost of a symmetry centre search. With elliptic profiles, the initial conditions can be eliminated by deconvoluting the images $F_0(x, y, t_{n>1})$ in the time series with the first image $F_0(x, y, t_0)$ using, *e.g.*, a Wiener filter. This recovers the fundamental solution $c_\delta(x, y, t_n)$ independently of the initially bleached profile.

4 Results

Following the analysis of sect. 3, non-Gaussian fluorescence recovery scans are to be expected when studying homeotropically aligned DNA-lipid lamellar complexes with a 2d nematic-like symmetry for the DNA fragments. We managed to get a fairly well oriented sample with the following composition: volume fractions of water, DNA and lipids equal to, respectively, 0.38, 0.15 and 0.47. The sample is macroscopically homogeneous and its small-angle X-ray scattering spectrum, with 4 sharp Bragg peaks in the ratio 1:2:3:4, is characteristic of a lamellar stacking of bilayers [39]. The sample also displays the typical broad line between the 2nd and 3rd order Bragg peaks usually interpreted as signalling the 2d nematic order of the DNA fragments confined within the water layer. Indeed, from X-rays the water channels are about 3.4 nm in thickness, implying that the rotational degrees of freedom for 50 nm long DNA rods are restricted to a two-dimensional space. The DNA volume fraction in *water*, that is to say $0.15/(0.15 + 0.38) = 28\%$, also exceeds by a fair margin the 2d overlap concentration —estimated here to be about 2.4% volume fraction— and a disordered DNA structure is very unlikely.

With this sample, we found fluorescence recovery scans departing significantly from a Gaussian profile in the tail region of the data. The non-Gaussian features in the long-time limit are strikingly illustrated in fig. 2, as a representative example.

On the contrary, data is much better described by the functional form of eq. (14), with now two distinct parameters for fitting the data. This is readily shown in fig. 3,

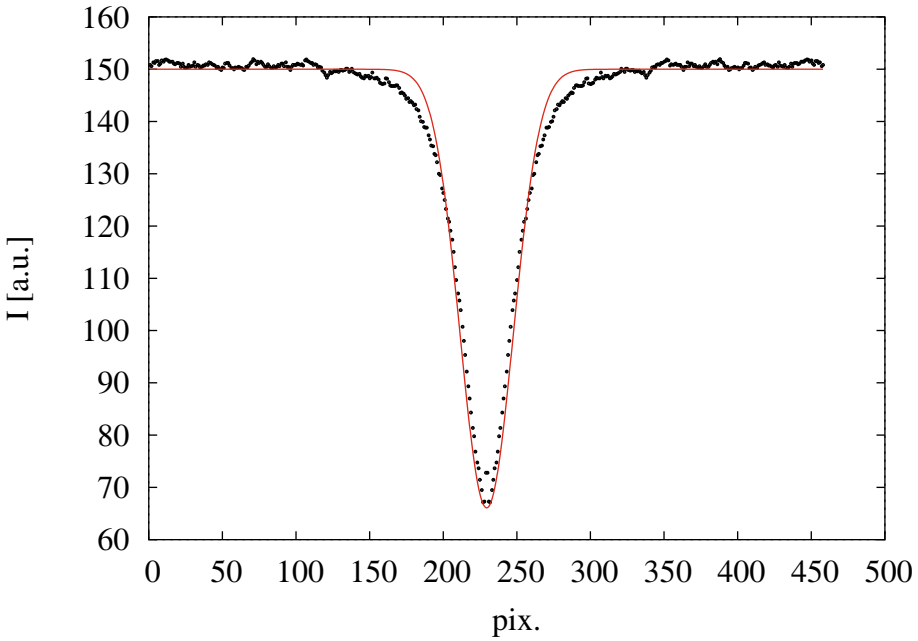

Fig. 2. Fluorescence recovery profile at time $t = 1320$ s after the photobleaching burst for an oriented domain in the ternary system with DNA content 0.15. The continuous line corresponds to the best fit to a Gaussian profile, with poor agreement in the tails of the profile.

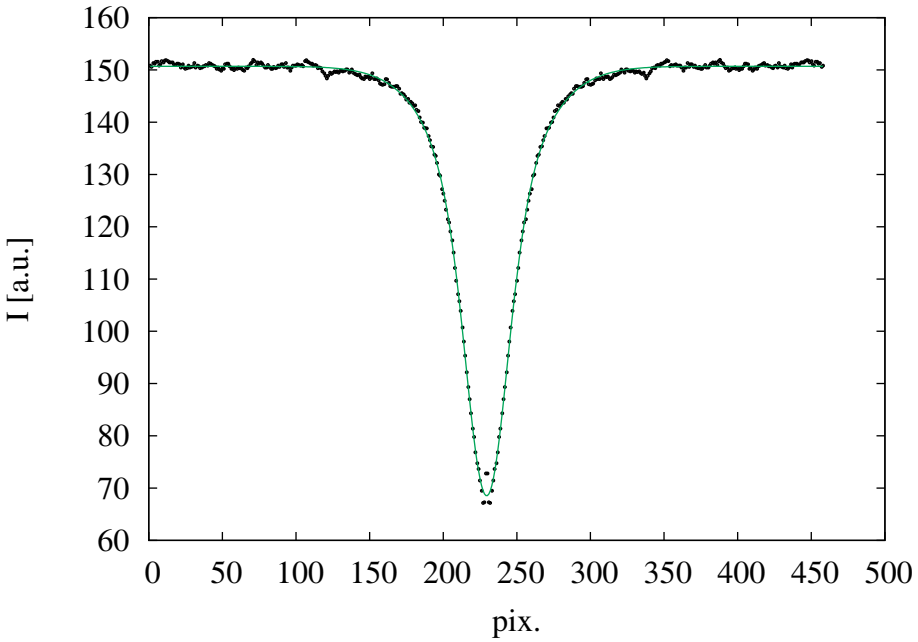

Fig. 3. Same fluorescence recovery profile as displayed in fig. 2. The continuous line corresponds to the best fit to the non-Gaussian profile involving the modified Bessel function of the first kind and integer order 0 —see eq. (14). The agreement is good both in the central and in the tail regions of the profile.

where the broader and more slowly decaying tails as compared to the Gaussian function are now satisfactorily accounted for in the same illustrative case.

Analysing profiles along a time series for a given bleached spot reveals that profiles departing from the Gaussian shape at time t systematically depart from the Gaussian shape at any later time $t' > t$. This indicates that the non-Gaussian shapes cannot be attributed to a saturation of the initial bleaching process —with $c_0(z)$ *non-linear* in $I(z)$— as this should also lead to a relaxation towards Gaussian shapes in the long-time limit.

Two parameters, defined at time t as the underlying variances of the anisotropic Gaussian profile for a given height z, and expressed from eq. (12) as, respec-

tively, $w_0^2/2 + 4D_\parallel t$ and $w_0^2/2 + 4D_\perp t$, can be extracted by analysing a time sequence of profiles.

For the data recorded in an oriented domain of the ternary sample, these variance parameters are plotted as a function of time in fig. 4.

The two obtained variances are clearly distinct at all times, which evidences, now in quantitative terms, the non-Gaussian shape of the fluorescence recovery profiles mentioned above. It should be noted that the variances are also distinct at $t = 0$, whereas the model description given by eq. (12) implies an initially *Gaussian* shape. Moreover, it has been observed that, at earlier times (up to $t \approx 250$ s in fig. 4), neither the Gaussian profile, nor our model involving the modified Bessel function are able to give a satisfactory description of the experimental data. We attribute this discrepancy to the crudeness of our approximate treatment in deriving the model but, as discussed in sect. 3 and, specifically, in view of the simulation results of sect. 3.3, this should not impair the model validity, at least in the long-time limit. As a matter of fact, fig. 4 indicates that the two variances are reasonably well fitted by laws linear in time for $t \geq 250$ s. Notwithstanding the model failure at (and near) $t = 0$, such a behaviour is the usual signature of Brownian dynamics. We therefore confidently consider the two slopes resulting from a data analysis based upon eq. (12) as directly related to the two diffusion coefficients $D_\parallel$ and $D_\perp$, with the larger value associated to the *a priori* easier and, therefore, faster *i.e.* lengthwise diffusive motion in the two-dimensionally confined nematic phase of DNA rods —see experimentally determined values in table 1.

With confidence in using eq. (12) as a legitimate tool for data analysis gained from the above-described results, we tentatively tried to extend the method to cholesteric domains in the binary DNA-solvent system, but checked first its consistency for the simpler case of an isotropic phase: Fluorescence recovery scans are expected to lead to Gaussian profiles at all times —see eq. (12) in the limit where $D_\parallel = D_\perp$. From a practical point of view, the recovery scans are also quite noisy in the low concentration part of the phase diagram where the isotropic phase is found because fluorescence is bound to be weak for dilute samples. In spite of this experimental limitation, Gaussian shapes are actually observed (data not shown) for isotropic samples. For a DNA concentration $c = 80$ mg/mL, *i.e.* at the upper limit of the isotropic phase, the analysis of the time series leads to $D_{\rm iso} = 25 \pm 2$ μm^2/s. Note that Gaussian shapes are also observed at higher concentrations where a phase separation occurs between the isotropic phase and more ordered structures, *provided that* an isotropic region has been selected for the measurement. As a representative example of this last case, the increase in time of the variance of the fitted Gaussian profile is displayed in fig. 5 for a sample with an overall DNA concentration[2] $c = 160$ mg/mL. The variance data is well described by a linear law and, from the isotropic limit of eq. (12), the slope corresponds to a unique translational diffusion coefficient $D_{\rm iso}$, with here a value found to be 0.13 ± 0.02 μm^2/s.

Table 1. Diffusion coefficients and dynamic anisotropies for several DNA-containing samples.

DNA vol. fraction (with respect to solvent)	$D_\parallel$ (μm^2/s)	$D_\parallel/D_\perp$
28.3% (DNA-lipid complex)	$2.7 \pm 0.2 \times 10^{-3}$	40.9 ± 4.5
20.5% (chol. phase)	$5.8 \pm 1.5 \times 10^{-2}$	14 ± 4
4.7% (iso. phase)	25 ± 2	1

At even higher concentrations the one-phase, cholesteric region of the phase diagram is reached. We have been able to get a well-oriented, planar domain (*i.e.* helical axis along the optical axis of the set-up) for a cholesteric sample with DNA composition $c = 350$ mg/mL. Quite remarkably, non-Gaussian fluorescence recovery scans have been found in this case and, here again, eq. (12) is in good agreement at all times with the experimental profiles (data not shown). The two variance parameters $w_{0\parallel}^2/2 + 4D_\parallel t$ and $w_{0\perp}^2/2 + 4D_\perp t$ have been extracted by analysing a time sequence of profiles, as was done previously with data from the DNA-lipid complex. They are plotted as a function of time in fig. 6. The corresponding values for the diffusion coefficients are $D_\parallel = 5.8 \pm 1.5 \times 10^{-2}$ μm^2/s and $D_\perp = 4.1 \pm 0.3 \times 10^{-3}$ μm^2/s , see also table 1. In such an already concentrated system (the DNA volume fraction is about 20%) the anisotropic ratio $D_\parallel/D_\perp = 14 \pm 4$ is rather high, with an overall significant slowing down of the Brownian motion as compared to the isotropic phase —see sect. 5 for a more detailed discussion.

It is interesting to note that, though cholesteric domains oriented such that the helical axis is parallel to the optical axis of the measurement set-up cannot be easily differentiated from isotropic domains using *polarised* microscopy —both appear uniformly dark between crossed polars— their signature in FRAP experiments is conspicuous. Indeed, we find experimentally in the case of samples located in the coexistence region of the phase diagram that distinct "dark domains" may be associated to either Gaussian fluorescence recovery profiles —for instance, data leading to fig. 5 in the case where 160 mg/mL— or to *non*-Gaussian ones. Our interpretation is that, in the former case, the bleaching spot irradiates a homogeneous, isotropic domain in a phase separated sample, whereas it reaches an oriented cholesteric domain in the latter case. Such an observation opens the possibility to study quite systematically concentration effects in the binary system. If it is indeed possible to bleach independently homogeneous domains belonging to separated phases in the same sample, Gaussian profiles on one hand and profiles involving the modified Bessel function on the other hand will be associated to three diffusion coefficients, namely $D_{\rm iso}$ for the locally segregated isotropic phase, and $D_\parallel$ and $D_\perp$

[2] Note that, though the phase separation occurs in a *nominally* binary system, the local concentrations within coexisting domains cannot be easily deduced form applying the lever rule owing to polydispersity in DNA fragment sizes.

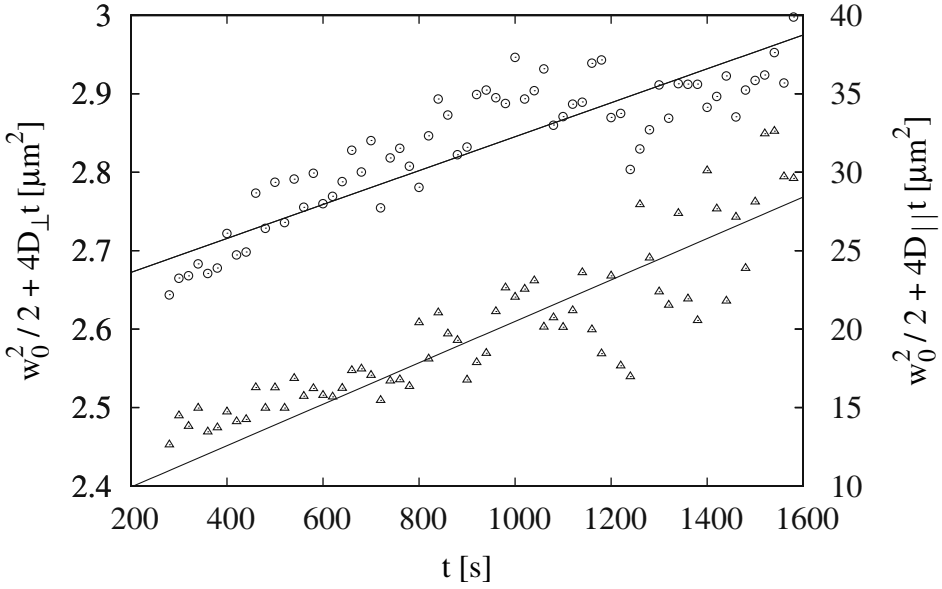

Fig. 4. Increase in time of the two variance parameters for an oriented domain in the ternary sample with DNA content 0.15 and 2d nematic order. The lines are linear fits to the data, leading to diffusion coefficient values $D_\parallel = 2.7 \pm 0.2\,10^{-3}$ μm^2/s ($\circ$, right scale) and $D_\perp = 6.6 \pm 0.5\,10^{-5}$ μm^2/s ($\triangle$, left scale).

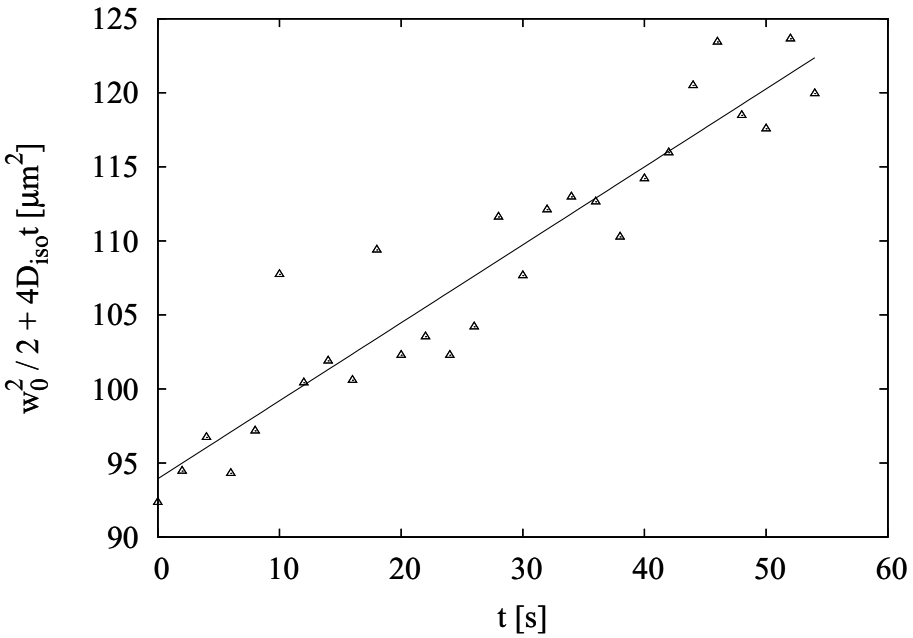

Fig. 5. Increase in time of the variance of the fluorescence recovery profile, fitted to a Gaussian function, for an isotropic domain in the phase-separated sample with an overall DNA concentration $c = 160$ mg/mL. The linear law (continuous line) fitted to the variance data points ($\triangle$ symbols) leads to a diffusion coefficient $D_{\rm iso} = 0.13 \pm 0.02$ μm^2/s.

for the cholesteric one, at a given (overall) concentration. Figure 7 provides a summary of the results obtained, using this approach, in the phase-separated region, as well as in the two one-phase regions of the phase diagram.

A general tendency —extending across the phase boundaries— for decreasing diffusion coefficients as the DNA concentration is increased is clearly observed in fig. 7. In addition, the diffusion coefficient *anisotropy* in cholesteric domains is apparently increasing with concentration, though experimental uncertainties somehow blur the results. The reader is referred to sect. 5 for a critical discussion about these results.

5 Discussion and conclusion

As illustrated in the previous section, the model introduced in sect. 3 proved to be adequate for analysing

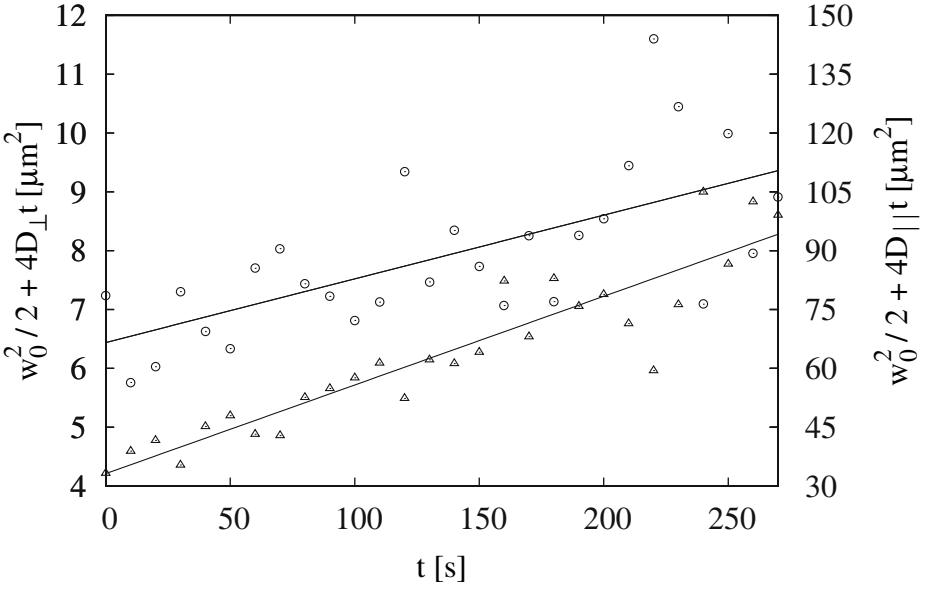

Fig. 6. Increase in time of the two variance parameters for an oriented cholesteric domain in the binary sample with $c = 350$ mg/mL. The straight lines are fits to the data, leading to diffusion coefficient values $D_{\|} = 5.8 \pm 1.5 \times 10^{-2}$ μm^2/s ($\circ$, right scale) and $D_{\perp} = 4.1 \pm 0.3 \times 10^{-3}$ μm^2/s ($\triangle$, left scale).

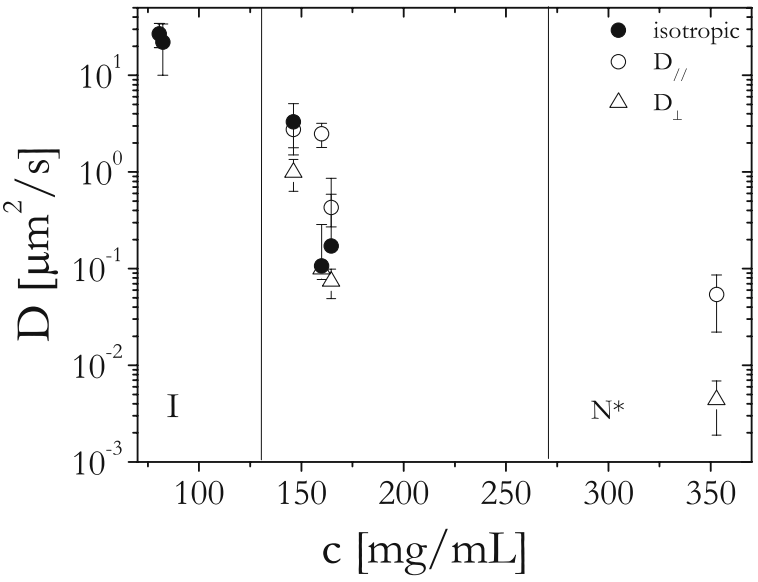

Fig. 7. Diffusion coefficients obtained by FRAP in the binary system as a function of DNA concentration c. The vertical lines separate a coexistence region from monophasic isotropic (I, low concentrations) and cholesteric (N*, high concentrations) domains. Within the coexistence region, c stands for the *overall* sample concentration. *Local* concentrations may significantly differ from the indicated nominal values. In cholesteric domains, the larger of the two measured diffusion coefficients is associated to the lenghtwise diffusion of the DNA fragments, *i.e.* $D_{\|}$ ($\circ$).

FRAP profiles in two kinds of systems similar in their local nematic symmetry for the Brownian particles, averaged along an axis perpendicular to the nematic director. Even though the averaging led to axially symmetric fluorescence recovery profiles, diffusion coefficients parallel and perpendicular to the nematic director could be extracted from the data.

In the DNA-lipid lamellar complex, concentration *and* confinement are both strong, as DNA volume fraction (with respect to solvent) and height of the solvent channel are, respectively, 28.3% and 3.4 nm, to be compared to the 2d overlap volume fraction 2.4% and DNA diameter *ca.* 2 nm. In the DNA-solvent system, concentration is the only control variable and the analogue of confinement, namely the helical pitch from a symmetry point of view, has not been varied in our study. Since the pitch is also quite large, we may tentatively consider the binary system as a kind of "unconfined" limit of the

ternary one. The increase in concentration from isotropic to cholesteric phase is clearly linked to a strong decrease in absolute values of the diffusion coefficients. Simultaneously, the dynamic anisotropy apparently increases with concentration in the cholesteric phase. The general trend is, qualitatively speaking, comparable to what has been observed in the cholesteric phase of *fd*-viruses by Lettinga *et al.* [19], observations also partially supported by recent computer simulations designed for such a system [21], though the dynamic anisotropy we find in the cholesteric phase ($D_{\parallel}/D_{\perp} = 14 \pm 4$) is roughly twice the one found experimentally for *fd*-viruses [19]. In addition, as far as absolute values are concerned, we observe a large difference between $D_{\rm iso}$ in the isotropic phase and the analogous quantity, namely $D_{\parallel}/3 + 2D_{\perp}/3$ in the cholesteric phase, with values (taken from table 1) 25 μm^2/s and $2.2\,10^{-2}$ μm^2/s for $c = 80$ mg/mL and $c = 350$ mg/mL, respectively, whereas similar values have been observed, and predicted by numerical simulations, on both sides of the two-phase domain for the *fd*-virus system [21]. Such a discrepancy may arise from the fact that our system has a less "model" character, owing to polydispersity as the most obvious difference, in comparison with the *fd*-virus system. As the order of magnitude for $D_{\rm iso}$ is compatible with theoretical expectations [3], polydispersity effects are presumably much stronger in the ordered phase.

In conclusion, it is also instructive to compare absolute values and dynamic anisotropies in the ternary DNA-lipid complex and the homogeneous cholesteric phase. The 2 samples are easily ordered in terms of increasing DNA volume fractions with respect to solvent, see again table 1.

Confinement of the DNA fragments by the lipid bilayers appears to be very effective in slowing down the Brownian motion of the particles, but the increase in dynamic anisotropy $D_{\parallel}/D_{\perp}$ may, tentatively, be ascribed to a concentration effect mainly, though more detailed investigations that are beyond the scope of this work would be required to firmly establish this point.

The authors warmly thank Annie Février for having processed and purified all the DNA fragments needed for the sample preparation. The authors are also very grateful to Dr. Sebastian Seiffert for having kindly provided the initial MATLAB routines that were used in this work, after being adapted by Andreas Schöppach. E.R.T.S. specially thanks the French Ministry of Foreign and European Affairs for an Eiffel-doctoral fellowship. This work was supported by the CAPES-CoFÉCUB French-Brazilian program under grant n °558/07.

References

1. S. Broersma, J. Chem. Phys. **32**, 1632 (1960).
2. M.M. Tirado, J.G. de la Torre, J. Chem. Phys. **71**, 2581 (1979).
3. M.M. Tirado, C.L. Martinez, J.G. de La Torre, J. Chem. Phys. **81**, 2047 (1984).
4. B.A. Scalettar, J.E. Hearst, M. P. Klein, Macromolecules **22**, 4550 (1989).
5. L. Wang, M.M. Garner, Hyuk Yu, Macromolecules **24**, 2368 (1991).
6. T. Nicolai, M. Mandel, Macromolecules **22**, 2348 (1989).
7. M.P.B. van Bruggen, H.N.W. Lekkerkerker, J.K.G. Dhont, Phys. Rev. E **56**, 4394 (1997).
8. J.K. Phalakornkul, A.P. Gast, R. Pecora, Macromolecules **32**, 3122 (1999).
9. S.A. Tatarkova, D.A. Berk, Phys. Rev. E **71**, 041913 (2005).
10. T. Odijk, Macromolecules **19**, 2073 (1986).
11. I. Teraoka, R. Hayakawa, J. Chem. Phys. **89**, 6989 (1988).
12. T. Sato, A. Teramoto, Macromolecules **24**, 193 (1991).
13. S. Szamel, Phys. Rev. Lett. **70**, 3744 (1993).
14. H. Löwen, Phys. Rev. E **50**, 1232 (1994).
15. J.K.G. Dhont, M.P.B. van Bruggen, W.J. Briels, Macromolecules **32**, 3809 (1999).
16. M.P.B. van Bruggen, H.N.W. Lekkerkerker, G. Maret, J.K.G. Dhont, Phys. Rev. E **58**, 7668 (1998).
17. S.V. Divinskikh, I. Furó, J. Chem. Phys. **115**, 1946 (2001).
18. S.V. Divinskikh, I. Furó, H. Zimmermann, A. Maliniak, Phys. Rev. E **65**, 061701 (2002).
19. M.P. Lettinga, E. Barry, Z. Dogic, Europhys. Lett. **71**, 692 (2005).
20. Y. Han, A.M. Alsayed, M. Nobili, J. Zhang, T.C. Lubensky, A.G. Yodh, Science **314**, 626 (2006).
21. M.P. Lettinga, J.K.G. Dhont, Z. Zhang, S. Messlinger, G. Gompper, Soft Matter **6**, 4556 (2010).
22. C.K. Yun, A.G. Fredricksen, Mol. Cryst. Liq. Cryst. **12**, 73 (1970).
23. K. Otnes, R. Pynn, J.A. Janik, J.M. Janik, Phys. Lett. A **38**, 335 (1972).
24. K.-S Chu, D.S. Moroi, J. Phys. (Paris) **36**, C199 (1975).
25. M. Allen, Phys. Rev. Lett. **65**, 2881 (1990).
26. Z. Zhang, H. Guo, J. Chem. Phys. **133**, 144911 (2010).
27. H. Maeda, Y. Maeda, Nano Lett. **7**, 3329 (2007).
28. D. Mukhija, M.J. Solomon, J. Colloid Interface Sci. **314**, 98 (2007).
29. J. Mathé, J.-M. Di Meglio, B. Tinland, J. Colloid Interface Sci. **322**, 315 (2008).
30. H. Uemura, M. Ichikawa, Y. Kimura, Phys. Rev. E **81**, 051801 (2010).
31. Y. Gambin, G. Massiera, L. Ramos, C. Ligoure, W. Urbach, Phys. Rev. Lett. **94**, 110602 (2005).
32. S. Seiffert, W. Oppermann, J. Microsc. **220**, 20 (2005).
33. P. Moreau, D. van Effenterre, L. Navailles, F. Nallet, D. Roux, Eur. Phys. J. E **26**, 225 (2008).
34. F. Lanni, B.R. Ware, Rev. Sci. Instrum. **53**, 905 (1982).
35. T.E. Strzelecka, R.L. Rill, Macromolecules **24**, 5124 (1991).
36. F. Livolant, A. Leforestier, Prog. Polym. Sci. **21**, 1115 (1996).
37. T. Pott, A. Colin, L. Navailles, D. Roux, Interface Sci. **11**, 249 (2003).
38. E. Andreoli de Oliveira, E.R. Teixeira da Silva, A. Février, É. Grelet, F. Nallet, L. Navailles, EPL **91**, 28001 (2010).
39. E.R. Teixeira da Silva, E. Andreoli de Oliveira, A. Février, F. Nallet, L. Navailles, Eur. Phys. J. E **34**, 83 (2011).
40. D.H. Van Winkle, M.W. Davidson, W.X. Chen, R.L. Rill, Macromolecules **23**, 4140 (1990).
41. P.C. Martin, O. Parodi, P.S. Pershan, Phys. Rev. A **6**, 2401 (1972).
42. D. Axelrod, D.E. Koppel, J. Schlessinger, E. Elson, W.W. Webb, Biophys. J. **16**, 1055 (1976).
43. G.I. Hauser, S. Seiffert, W. Oppermann, J. Microsc. **230**, 353 (2008).